

**Quasi-2D Hybrid Perovskite Formation Using Benzothieno[3,2-b]Benzothiophene (BTBT) Ammonium Cations
Substantial Cesium Lead(II) Iodide Black Phase Stabilization**

Denis, Paul Henry; Mertens, Martijn; Van Gompel, Wouter T.M.; Maufort, Arthur; Mertens, Sigurd; Wei, Zimu; Van Landeghem, Melissa; Gielen, Sam; Grozema, Ferdinand; More Authors

DOI

[10.1002/adom.202200788](https://doi.org/10.1002/adom.202200788)

Publication date

2022

Document Version

Final published version

Published in

Advanced Optical Materials

Citation (APA)

Denis, P. H., Mertens, M., Van Gompel, W. T. M., Maufort, A., Mertens, S., Wei, Z., Van Landeghem, M., Gielen, S., Grozema, F., & More Authors (2022). Quasi-2D Hybrid Perovskite Formation Using Benzothieno[3,2-b]Benzothiophene (BTBT) Ammonium Cations: Substantial Cesium Lead(II) Iodide Black Phase Stabilization. *Advanced Optical Materials*, 10(18). <https://doi.org/10.1002/adom.202200788>

Important note

To cite this publication, please use the final published version (if applicable).
Please check the document version above.

Copyright

Other than for strictly personal use, it is not permitted to download, forward or distribute the text or part of it, without the consent of the author(s) and/or copyright holder(s), unless the work is under an open content license such as Creative Commons.

Takedown policy

Please contact us and provide details if you believe this document breaches copyrights.
We will remove access to the work immediately and investigate your claim.

Green Open Access added to TU Delft Institutional Repository

'You share, we take care!' - Taverne project

<https://www.openaccess.nl/en/you-share-we-take-care>

Otherwise as indicated in the copyright section: the publisher is the copyright holder of this work and the author uses the Dutch legislation to make this work public.

Quasi-2D Hybrid Perovskite Formation Using Benzothieno[3,2-*b*]Benzothiophene (BTBT) Ammonium Cations: Substantial Cesium Lead(II) Iodide Black Phase Stabilization

Paul-Henry Denis, Martijn Mertens, Wouter T. M. Van Gompel, Arthur Maufort, Sigurd Mertens, Zimu Wei, Melissa Van Landeghem, Sam Gielen, Bart Ruttens, Davy Deduytsche, Christophe Detarvernier, Laurence Lutsen, Ferdinand Grozema, Koen Vandewal, and Dirk Vanderzande*

3D hybrid perovskites (APbX₃) have made a significant impact on the field of optoelectronic materials due to their excellent performance combined with facile solution deposition and up-scalable device fabrication. Nonetheless, these materials suffer from environmental instability. To increase material stability, the organic cation (A) is substituted by the non-volatile cesium cation. However, the desired photoactive cesium lead(II) iodide black phase is metastable in ambient conditions and spontaneously converts into the photo-inactive yellow δ -phase. In this work, the black phase is stabilized by the formation of a quasi-2D perovskite containing a benzothieno[3,2-*b*]benzothiophene (BTBT) large organic ammonium cation. Thermal analysis shows that degradation of the butylammonium (BA)-based quasi-2D perovskite (BA)₂CsPb₂I₇ sets in at ≈ 130 °C, while (BTBT)₂CsPb₂I₇ is phase-stable until ≈ 230 °C. Additionally, the (BTBT)₂CsPb₂I₇ film does not show any sign of degradation after exposure to 77% Relative Humidity in the dark for 152 days, while (BA)₂CsPb₂I₇ degrades in a single day. Photoconductor-type detectors based on (BTBT)₂CsPb₂I₇ demonstrate an increased external quantum efficiency and a similar specific detectivity compared to the BA-based reference detectors. The results demonstrate the utility of employing a BTBT cation within the organic layer of quasi-2D perovskites to significantly enhance the stability while maintaining the optoelectronic performance.

1. Introduction

3D hybrid perovskites with the chemical formula ABX₃ (with monovalent small organic cation A, divalent metal B, and halide X) emerged as an attractive light harvester for optoelectronic applications.^[1,2] Perovskite solar cells, for instance, have known an unprecedented performance improvement over the last decade, reaching a record efficiency of 25.7%.^[3] Despite these spectacular performances, the intrinsic environmental instability of 3D hybrid perovskites hampers their commercial application. The moisture sensitivity and thermal instability of the 3D hybrid perovskite MAPbI₃^[4–6] are partly related to the volatility of the small methylammonium (MA) cation. When substituted by another small organic cation, formamidinium (FA), the resulting perovskite FAPbI₃ displays a higher decomposition temperature than its MA-based counterpart, however, still with a pronounced sensitivity toward humidity.^[4,7–10]

P.-H. Denis, M. Mertens, W. T. M. Van Gompel, A. Maufort, S. Mertens, M. Van Landeghem, S. Gielen, B. Ruttens, L. Lutsen, K. Vandewal, D. Vanderzande
Institute for Materials Research (IMO)
UHasselt – Hasselt University
Agoralaan 1 – Building D, Diepenbeek 3590, Belgium
E-mail: dirk.vanderzande@uhasselt.be

P.-H. Denis, M. Mertens, W. T. M. Van Gompel, A. Maufort, S. Mertens, M. Van Landeghem, S. Gielen, B. Ruttens, L. Lutsen, K. Vandewal, D. Vanderzande
IMEC
Associated lab IMOMEC
Wetenschapspark 1, Diepenbeek 3590, Belgium

Z. Wei, F. Grozema
Grozema group
TUDelft
Van der Maasweg 9, HZ Delft 2639, The Netherlands
D. Deduytsche, C. Detarvernier
CoCooN
Ghent University
Krijgslaan 281/S1, Gent B-9000, Belgium

 The ORCID identification number(s) for the author(s) of this article can be found under <https://doi.org/10.1002/adom.202200788>.

DOI: 10.1002/adom.202200788

As a result, the inorganic cesium (Cs^+) cation has been selected as an alternative nonvolatile species to address the stability issues, yielding the all-inorganic CsPbX_3 ($X = \text{Cl, Br, and I}$) with excellent thermal stability.^[11–13] However, the black CsPbI_3 α -phase with a suitable bandgap of 1.73 eV is metastable below 320 °C in ambient conditions, converting spontaneously into a yellow, photo-inactive, non-perovskite δ -phase.^[14,15] In addition, β and γ black phase polymorphs have also been encountered besides the α -phase.^[16,17] To benefit from the photoactivity of the CsPbI_3 black phase in device applications, it is necessary to improve its phase stability. Some recent approaches toward the phase stabilization of the cesium lead(II) iodide α -phase include halogen exchange,^[11,18,19] solvent engineering,^[20] and the use of a bication component system.^[15] While progress has been made, the phase stability of CsPbI_3 -containing films still needs to be further improved.

The formation of quasi-2D Ruddlesden–Popper hybrid perovskites $(\text{A}')_2\text{A}_{n-1}\text{B}_n\text{X}_{3n+1}$ (with a large organic ammonium cation A' , small ammonium cation A , divalent metal cation B , and halide X) has proven to be a practical approach to obtain highly durable perovskite materials.^[21–24] Their optoelectronic properties can be systematically tuned by applying the corresponding precursor components in the correct stoichiometric ratio, hereby varying the number of consecutive inorganic layers (n) separated by organic layers.^[4,22,25,26] In that respect, a similar approach has been followed to stabilize cesium lead(II) iodide.

Liao et al.^[27] initially reported the formation of the cesium lead(II) iodide quasi-2D hybrid perovskite $(\text{BA})_2\text{CsPb}_2\text{I}_7$ through the incorporation of an aliphatic butyl ammonium (BA) cation. This layered $\langle n \rangle = 2$ hybrid perovskite displayed excellent stability under 30% relative humidity (RH) exposure at 25 °C for 2 months and thermal stress at 85 °C for 3 days. Soon after, the aromatic phenyl ethyl ammonium (PEA) cation was systematically introduced into $\gamma\text{-CsPbI}_3$ by Jiang et al.^[28] to yield a series of quasi-2D hybrid perovskites $(\text{PEA})_2\text{Cs}_{n-1}\text{Pb}_n\text{I}_{3n+1}$ with $\langle n \rangle = 1, 3, 5, 10, 40,$ and 60 . The undesirable yellow orthorhombic δ -phase could be considerably suppressed in the quasi-2D perovskites under an ambient atmosphere compared to the 3D counterpart.

In practice, it has been challenging to form phase-pure $\langle n \rangle$ quasi-2D hybrid perovskite thin films. When a particular layered n hybrid perovskite is targeted, usually a broad distribution of various coexistent layer thicknesses n is present within the film.^[29,30] Due to this layer thickness distribution, charge carrier transport within quasi-2D hybrid perovskite films tends to be more complex compared to their pure 3D counterpart.^[31,32] It is, therefore, favorable to synthesize quasi-2D hybrid perovskite films with enhanced phase purity. In particular, Hadi et al.^[33] demonstrated the influence of strongly complexing solvents on the phase-purity of quasi-2D $\text{BA}_2\text{Cs}_{n-1}\text{Pb}_n\text{I}_{3n+1}$ films. By establishing iodoplumbate/solvent complexes, a retardation of the crystallite nucleation rate was achieved, which yielded improved phase purity, crystallinity, and film morphology.

Although it has been shown that simple aliphatic or aromatic ammonium cations (e.g., BA or PEA) can be applied toward the stabilization of the cesium lead(II) iodide black phase through dimension engineering, the insertion of more complex organic ammonium cations, potentially bestowing additional optical

properties^[34–36] and charge carrier dynamics to the hybrid,^[37–42] has not been applied for the same purpose. In addition, approaches to increase the phase purity of quasi-2D hybrid perovskite films have been poorly investigated to date.

In this work, we assess the cesium lead(II) iodide black phase stabilization by a polyheterocyclic aromatic benzothieno[3,2-*b*]benzothiophene (BTBT) cation through quasi-2D hybrid perovskite formation and compare its stabilization effect with the state-of-the-art aliphatic BA cation. Our motivation for the choice of BTBT as an organic cation for quasi-2D perovskites is twofold. First, derivatives of BTBT have shown considerable charge carrier mobility values in organic electronics.^[43] Second, we hypothesized that the rigid molecular structure of the BTBT cation, with its fused ring system, might enhance the stability of the perovskite compared to the flexible BA cation.

Using (in situ) XRD and UV–vis spectroscopy, we find that both the thermal and moisture stability of the $(\text{BTBT})_2\text{CsPb}_2\text{I}_7$ thin film are vastly superior with respect to the reference $(\text{BA})_2\text{CsPb}_2\text{I}_7$ thin film. Time-resolved microwave conductivity (TRMC) measurements reveal that the photoconductivity and charge-carrier diffusion lengths for a $(\text{BTBT})_2\text{CsPb}_2\text{I}_7$ thin film are slightly increased with respect to the $(\text{BA})_2\text{CsPb}_2\text{I}_7$ thin film. Moreover, $(\text{BTBT})_2\text{CsPb}_2\text{I}_7$ -based photoconductor-type detectors delivered a higher photocurrent, higher external quantum efficiency (EQE) and similar specific detectivity compared to $(\text{BA})_2\text{CsPb}_2\text{I}_7$ -based ones. We attribute the enhanced photocurrent and EQE to the higher crystallinity and bigger crystallite size of the $(\text{BTBT})_2\text{CsPb}_2\text{I}_7$ thin film with respect to $(\text{BA})_2\text{CsPb}_2\text{I}_7$. Our work clearly demonstrates the benefit of employing a large polyheterocyclic aromatic ammonium cation in quasi-2D hybrid perovskites for stable and efficient solution-processable optoelectronics.

2. Results and Discussion

2.1. Optical, Structural, and Morphological Properties

The mono-functionalized BTBT with a propyl ammonium tethering chain (BTBT) was synthesized according to our previously reported procedure (Figure S1, Supporting Information).^[44] The commercially available *n*-butylamine hydroiodide (BAI) was purified by precipitation from methanol in diethyl ether before use. For the quasi-2D hybrid perovskite films $(\text{BA})_2\text{CsPb}_2\text{I}_7$ and $(\text{BTBT})_2\text{CsPb}_2\text{I}_7$ (Figure 1a), $\langle n \rangle = 2$ will be used to denote the targeted nominal composition based on the stoichiometry of the precursor solution. Contrastingly, n will be used to denote a specific quasi-2D hybrid perovskite $(\text{A}')_2\text{A}_{n-1}\text{B}_n\text{X}_{3n+1}$ with a number of layers (n) present in the targeted $\langle n \rangle = 2$ thin film, as usually a distribution of different layers is present.

Both $(\text{BA})_2\text{CsPb}_2\text{I}_7$ and $(\text{BTBT})_2\text{CsPb}_2\text{I}_7$ films were optimized toward optimal crystallinity and phase purity. This requires the use of a different procedure for these two perovskite materials due to the significant differences in the molecular structure of the organic cations. The precursor solution of $(\text{BA})_2\text{CsPb}_2\text{I}_7$ with a 0.3 M concentration was spin-coated and thermally annealed at 130 °C. It was shown in the literature that by adding a solvent with high complexation strength to the precursor solution, the phase purity of a $(\text{BA})_2\text{CsPb}_2\text{I}_7$ thin film

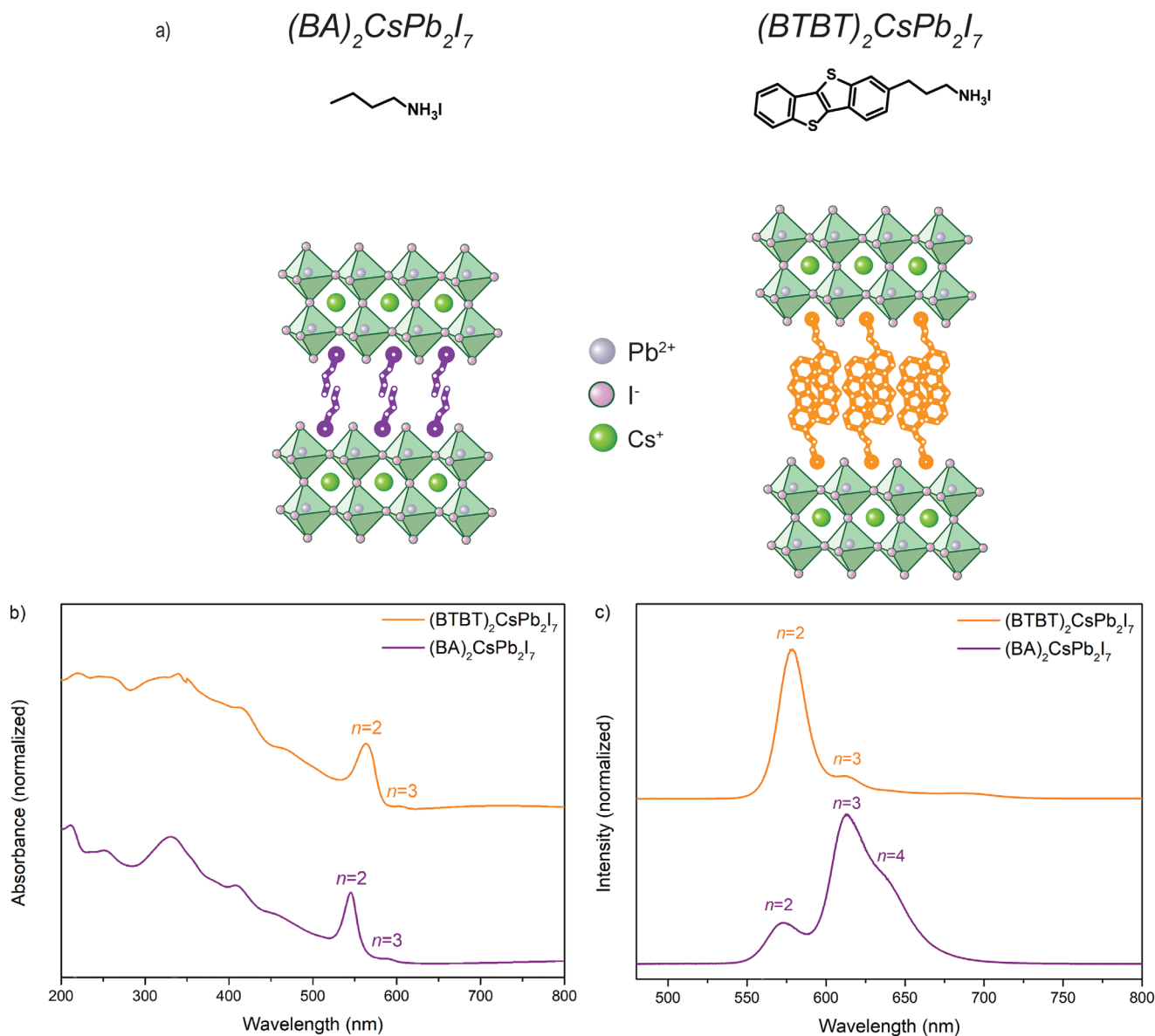


Figure 1. a) Schematic representation of the quasi-2D hybrid perovskite structures of $(BA)_2CsPb_2I_7$ and $(BTBT)_2CsPb_2I_7$. b) Absorption and c) emission spectra of a spin-coated $(BA)_2CsPb_2I_7$ thin film thermally annealed at 130 °C for 10 min, and a $(BTBT)_2CsPb_2I_7$ thin film solvent-annealed at 210 °C for 5 min. The emission spectra were obtained by exciting the samples at 405 nm.

could be improved.^[33] We, therefore, added a small amount of dimethylacetamide (DMAC) to the $(BA)_2CsPb_2I_7$ precursor solution in DMF to inhibit quasi-3D perovskite formation and favor the crystallization toward the targeted layered $n = 2$ hybrid perovskite. To obtain highly crystalline $(BTBT)_2CsPb_2I_7$ thin films, our previously reported thermal/solvent vapor annealing method was employed using DMSO to enhance the mobility of the rigid BTBT molecules during self-assembly.^[44] This annealing method cannot be applied to the BA-containing quasi-2D hybrid perovskite due to the dissolution of the respective thin films in the DMSO vapor environment. Peculiarly, a relatively high annealing temperature of 210 °C was required to obtain highly crystalline $(BTBT)_2CsPb_2I_7$ thin films. We suggest that the formation energy of a $(BTBT)_2CsPb_2I_7$ thin film is

significantly higher in contrast to that of $(BA)_2CsPb_2I_7$ due to the limited mobility of the bulky BTBT molecules compared to the small and flexible BA molecules.

The resulting absorption and emission spectra of the quasi-2D hybrid perovskite thin films are shown in Figure 1b,c.

The absorption spectra show that the layered $n = 2$ hybrid perovskites are successfully synthesized based on the appearance of the distinct excitonic absorption peaks at respectively 546 nm for $(BA)_2CsPb_2I_7$,^[33] and 565 nm for $(BTBT)_2CsPb_2I_7$ (Figure 1b). The optical properties of the previously reported $n = 1$ 2D layered perovskite $(BTBT)_2PbI_4$ were added to the supporting information for comparison (Figure S4, Supporting Information).^[44] The difference in excitonic peak position corresponding to a certain n value is attributed to the nature of the

large (BA or BTBT) organic cation, inducing a different degree of distortion of the interconnected corner-sharing lead(II) iodide octahedra.^[45] Besides $n = 2$, the excitonic peak corresponding to $n = 3$ is also visible in the absorption spectrum for each sample, though with a much lower intensity relative to $n = 2$.

Photoluminescence (PL) emission spectra reveal additional information concerning the presence of different phases within the thin film samples (Figure 1c). As expected, the PL spectra exhibit characteristic excitonic emission peaks that are slightly red-shifted compared to the corresponding absorption peaks. The $(\text{BA})_2\text{CsPb}_2\text{I}_7$ thin film contains emission peaks corresponding to a distribution of layer thicknesses ($n = 2, 3$, and 4), with emission primarily originating from the layered $n = 3$ hybrid perovskite. For the $(\text{BTBT})_2\text{CsPb}_2\text{I}_7$ thin film, the emission originates mainly from the layered $n = 2$ hybrid perovskite, accompanied by a very weak emission signal of the layered $n = 3$ hybrid perovskite and quasi-3D cesium lead(II) iodide (650–700 nm). We suggest that the appearance of this prominent $n = 2$ excitonic peak is likely due to the relatively low amount of layered $n = 3$ perovskite with respect to $n = 2$ present in the $(\text{BTBT})_2\text{CsPb}_2\text{I}_7$ film. However, the occurrence of energy funneling toward higher n phases, with the lowest band gap energy, makes a quantitative determination of the ratio between $n = 2$ and $n = 3$ phases difficult.^[46]

To assess the overall crystallinity of the samples, the XRD patterns of the spin-coated thin films are presented in Figure 2.

The diffraction patterns consist of a series of (0k0) reflections characteristic for a layered $n = 2$ hybrid perovskite with a preferential growth along the [101] direction, parallel to the substrate surface.^[26] The XRD pattern of our $(\text{BA})_2\text{CsPb}_2\text{I}_7$ film closely matches with those reported in the literature.^[33] The interplanar d_{0k0} spacing values of $(\text{BA})_2\text{CsPb}_2\text{I}_7$, and $(\text{BTBT})_2\text{CsPb}_2\text{I}_7$ are determined to be 19.6 and 31.6 Å, respectively. With respect to our previously reported $n = 1$ 2D layered perovskite $(\text{BTBT})_2\text{PbI}_4$ thin films (Figure S5, Supporting Information),^[44] the d spacing increases by almost 6 Å for $n = 2$ $(\text{BTBT})_2\text{CsPb}_2\text{I}_7$. This increase matches exactly with the addition of one lead(II) iodide octahedral sheet to $(\text{BTBT})_2\text{PbI}_4$, as expected.^[22,47,48]

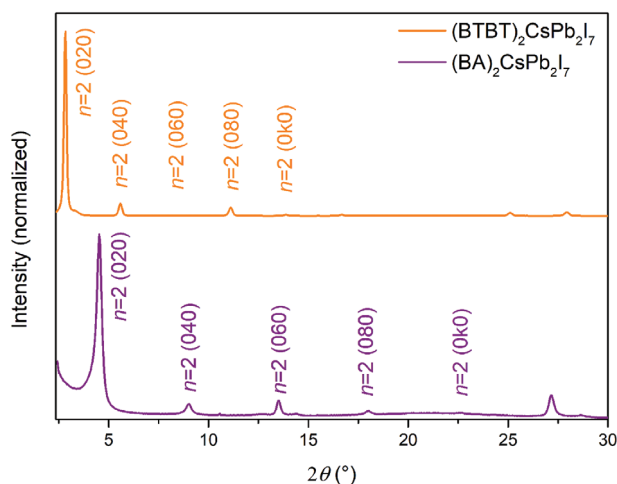


Figure 2. X-ray diffraction pattern of a spin-coated $(\text{BA})_2\text{CsPb}_2\text{I}_7$ thin film thermally annealed at 130 °C for 10 min, and a $(\text{BTBT})_2\text{CsPb}_2\text{I}_7$ thin film solvent annealed at 210 °C for 5 min.

The crystallite size (D) in both $(\text{BTBT})_2\text{CsPb}_2\text{I}_7$ and $(\text{BA})_2\text{CsPb}_2\text{I}_7$ thin films was estimated using Scherrer's equation, based on the FWHM of the first reflection:

$$D = \frac{K\lambda}{\beta \cos\theta} \quad (1)$$

with D the crystallite size, K a constant (shape factor, taken here as 1 for crystallites of an unknown shape), λ the wavelength of the X-ray, β the FWHM of the reflection (in radians), and θ the diffraction angle.^[49] The crystallite sizes of $(\text{BTBT})_2\text{CsPb}_2\text{I}_7$ and $(\text{BA})_2\text{CsPb}_2\text{I}_7$ were calculated to be 57 and 12 nm, respectively.

The thin film morphology and roughness of the films were examined by scanning electron microscopy (SEM) and atomic force microscopy (AFM), respectively, and the results are represented in Figure S6, Supporting Information. The SEM micrographs of $(\text{BA})_2\text{CsPb}_2\text{I}_7$ and $(\text{BTBT})_2\text{CsPb}_2\text{I}_7$ reveal full surface coverage with no pinholes. For $(\text{BTBT})_2\text{CsPb}_2\text{I}_7$, we observe a higher surface roughness based on AFM, in contrast to the smoother $(\text{BA})_2\text{CsPb}_2\text{I}_7$ thin film. The higher surface roughness of $(\text{BTBT})_2\text{CsPb}_2\text{I}_7$ compared to $(\text{BA})_2\text{CsPb}_2\text{I}_7$ can be attributed to the use of the solvent vapor annealing instead of the traditional thermal annealing method, inducing a different microstructure with bigger grains.

2.2. Thermal Stability

In situ temperature-controlled XRD measurements were carried out to study the intrinsic thermal stability of $(\text{BTBT})_2\text{CsPb}_2\text{I}_7$ and to compare it with the state-of-the-art $(\text{BA})_2\text{CsPb}_2\text{I}_7$ thin film (Figure 3). In this way, we investigate the effect of the addition of a polyheterocyclic aromatic ammonium cation on the cesium lead(II) iodide black phase stabilization with respect to the aliphatic BA one. The samples were heated with incremental steps of 1 °C min⁻¹ until complete degradation, and XRD patterns were acquired every 10 °C.

From the 2D in situ XRD plot, it is apparent that the $(\text{BA})_2\text{CsPb}_2\text{I}_7$ thin film is thermally stable until a temperature of ≈130 °C (Figure 3a). Above this temperature, the (0k0) reflections of the layered $n = 2$ hybrid perovskites start to decrease in intensity due to degradation into lead(II) iodide (inset diffractogram Figure 3b: main reflection at ≈12.6° 2θ).^[50] When the aliphatic BA cation is substituted with the BTBT cation, the thermal stability is dramatically enhanced to 230 °C, since no decrease in the intensity of the reflections nor the appearance of reflections corresponding to a degradation phase is apparent below this temperature (Figure 3c,d). The in situ XRD patterns with normalized intensities are shown in the Supporting Information (Figure S7, Supporting Information) to be able to investigate the much weaker reflections present at high temperatures that are obscured in the plot with absolute intensities, revealing the degradation of the cesium lead(II) iodide black phase into the yellow $\delta\text{-CsPbI}_3$ phase (reflection at ≈9.85° 2θ in diffractogram)^[28,51] at respectively 180 °C for $(\text{BA})_2\text{CsPb}_2\text{I}_7$ and 270 °C for $(\text{BTBT})_2\text{CsPb}_2\text{I}_7$. We suggest that the markedly enhanced stability has its origin in the rigid fused nature of the BTBT cation as compared to the more flexible BA. To study the influence of the organic cation in more detail, a thermal

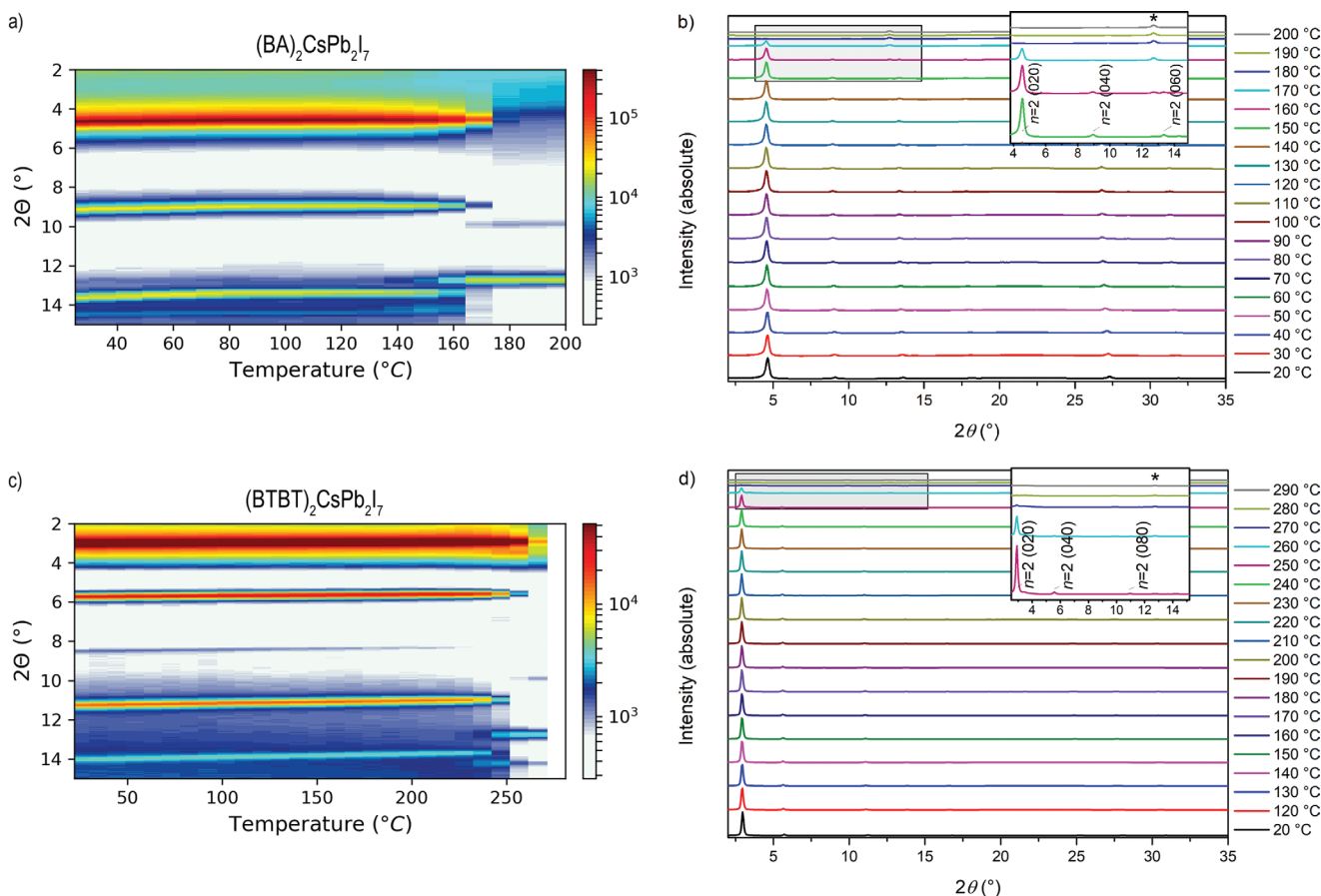


Figure 3. 2D in situ X-ray diffraction plots as a function of temperature starting from a spin-coated a) $(\text{BA})_2\text{CsPb}_2\text{I}_7$ and c) $(\text{BTBT})_2\text{CsPb}_2\text{I}_7$ thin film before the in situ experiment. In situ X-ray diffraction patterns (absolute intensity) as a function of temperature starting from a spin-coated b) $(\text{BA})_2\text{CsPb}_2\text{I}_7$ and d) $(\text{BTBT})_2\text{CsPb}_2\text{I}_7$ thin film before the in situ experiment. The weak reflections of the degradation product PbI_2 (*) are magnified in the respective temperature range.

gravimetric analysis (TGA) was performed on powders of the BAI and BTBTI ammonium iodide salts, probing the thermal stability of these large organic ammonium cations exclusively (Figure S8, Supporting Information). The aliphatic BAI salt shows gradual degradation weight loss under thermal stress starting from RT until ≈ 175 °C, whereafter a significant weight loss is observed that may be ascribed to decomposition of the ammonium salt followed by volatilization of butylamine and hydrogen iodide. In contrast, the BTBTI salt reveals no weight loss up to a temperature of almost 260 °C, indicating that the organic ammonium cation remains intact at such high temperatures. We therefore demonstrate that the introduction of a polyheterocyclic aromatic BTBT cation through quasi-2D hybrid perovskite formation effectively stabilizes the cesium lead(II) iodide black phase under thermal stress with respect to an aliphatic one, generating a highly stable active material for optoelectronics.

2.3. Moisture Stability

Encouraged by the superior intrinsic thermal stability of the $(\text{BTBT})_2\text{CsPb}_2\text{I}_7$ thin film (230 °C) as compared to the

state-of-the-art reference $(\text{BA})_2\text{CsPb}_2\text{I}_7$ (130 °C), we decided to study the intrinsic moisture stability of the samples over the course of 152 days under air of 77% relative humidity (RH) in the dark and at room temperature. The UV–vis absorption spectra and normalized XRD patterns of the samples at different times are summarized in Figure 4. For the $(\text{BA})_2\text{CsPb}_2\text{I}_7$ thin film, we observe degradation of the layered $n = 2$ hybrid toward the $n = 1$ 2D layered perovskite $(\text{BA})_2\text{PbI}_4$ ^[52] already after 1 day (excitonic absorption peak at 510 nm, Figure 4a; d spacing: 13.8 Å, Figure 4b). Additionally, degradation into the yellow δ -phase of CsPbI_3 (absorption peak around 410–420 nm;^[12] reflection at $\approx 9.85^\circ$ 2θ in diffractogram), PbI_2 (main reflection at $\approx 12.6^\circ$ 2θ in diffractogram) and a potential 1D hybrid phase^[53] (with an excitonic absorption peak at 413 nm; d spacing: 10.3 Å), occurs. After 1 month of storage, the $n = 1$ 2D layered perovskite $(\text{BA})_2\text{PbI}_4$ and the potential 1D hybrid phase have degraded completely into primarily lead(II) iodide (evinced by the increase of the intensity of the reflection at $\approx 12.6^\circ$ 2θ in the diffractogram) and the yellow δ -phase of CsPbI_3 .

In contrast, our $(\text{BTBT})_2\text{CsPb}_2\text{I}_7$ thin film shows excellent resistance against humidity, with no apparent degradation into lead(II) iodide nor a phase transition toward the yellow δ -phase over a period of 152 days, maintaining the excitonic absorption

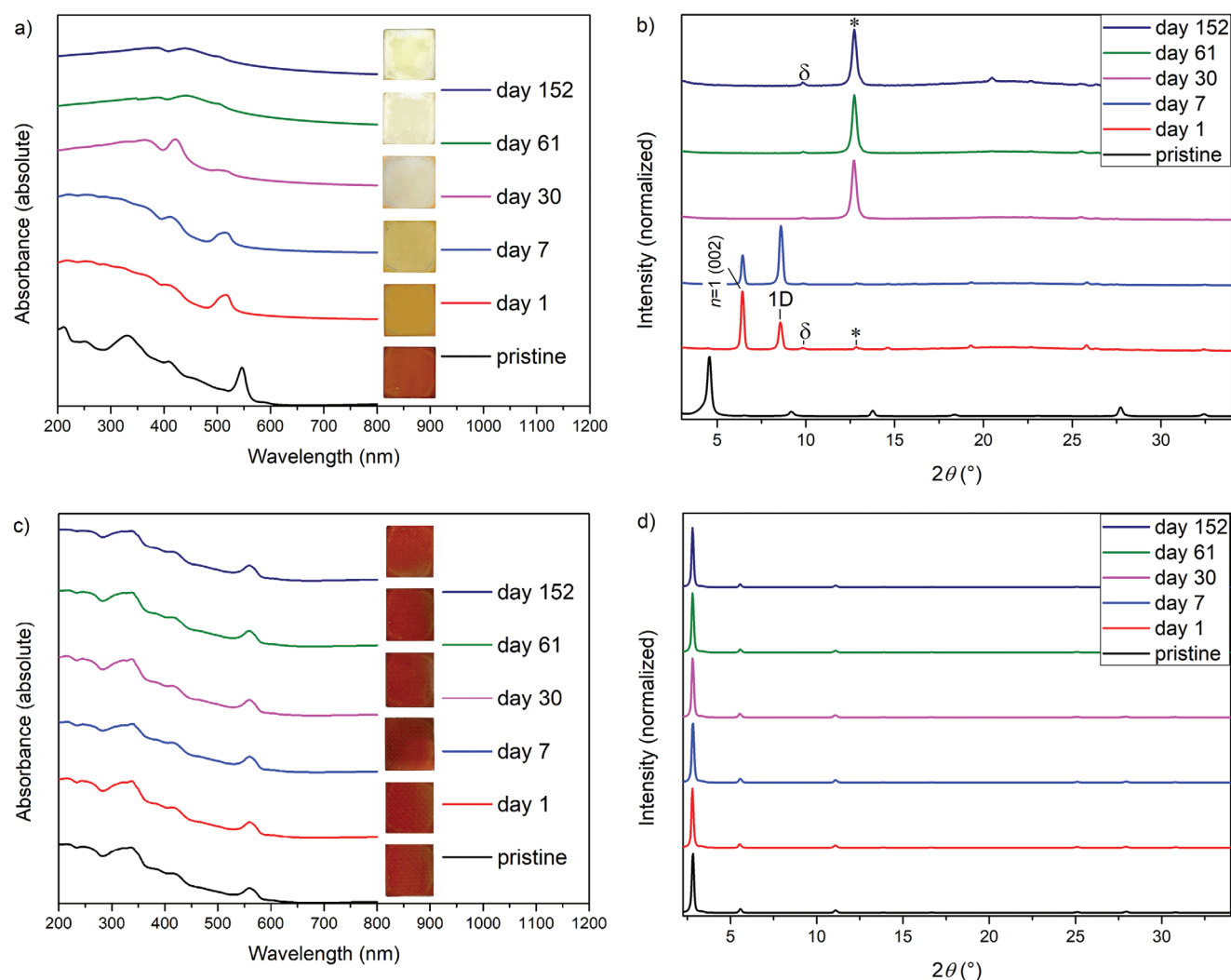


Figure 4. a) Absorption spectra of a spin-coated (BA)₂CsPb₂I₇ thin film that was prepared by annealing at 130 °C for 10 min, and c) of a (BTBT)₂CsPb₂I₇ thin film that was prepared by solvent annealing at 210 °C for 5 min. Normalized X-ray diffraction patterns of b) (BA)₂CsPb₂I₇ and d) (BTBT)₂CsPb₂I₇ thin films prepared using the same procedure as those used for the absorption spectroscopy measurements. The samples were stored at 77% RH and measured at different times over the course of 152 days. The weak reflections in the XRD patterns belonging to the degradation product PbI₂ (*) and the yellow δ phase (δ) are indicated in the relevant temperature range for (BA)₂CsPb₂I₇. For (BTBT)₂CsPb₂I₇, these reflections are absent after 152 days of storage.

peak at 565 nm (Figure 4c) and intense (0k0) reflections in the diffractogram corresponding to a *d* spacing of 31.6 Å that is characteristic for the layered *n* = 2 (BTBT)₂CsPb₂I₇ hybrid perovskite (Figure 4d). We propose that the introduction of polyheterocyclic aromatic BTBT molecules increases the hydrophobicity and rigidity of the organic layers compared to the aliphatic BA-containing ones, resulting in enhanced moisture stability and the inhibition of yellow δ-phase formation.^[54] The in situ XRD patterns of the moisture stability test with absolute intensities are shown in the ESI for completeness (Figure S9, Supporting Information).

To further investigate the moisture stability of the (BTBT)₂CsPb₂I₇ and (BA)₂CsPb₂I₇ thin films, water contact angles were determined. For (BTBT)₂CsPb₂I₇ films, the instantaneous contact angle was determined to be 81° ± 1°. For (BA)₂CsPb₂I₇ films, the instantaneous contact angle was more difficult to determine accurately due to the rapid decrease

in the angle upon contact of the water droplet with the film. An instantaneous contact angle of ≈64° could be determined. This angle decreases rapidly to a value of ≈23°. After the droplets have evaporated, the appearance of the thin films differs markedly for (BTBT)₂CsPb₂I₇ compared to (BA)₂CsPb₂I₇. While (BTBT)₂CsPb₂I₇ films (Figure S10a, Supporting Information) retain a dark color, that can be related to the perovskite phase, at the locations where the water droplets were dispensed, this is not the case for (BA)₂CsPb₂I₇ films. For (BA)₂CsPb₂I₇ (Figure S10b, Supporting Information), it is apparent that the water droplets dissolved the perovskite with the formation of (yellow) lead iodide as a result. Video files of the contact angle measurements are available in the Supporting Information.

As indicated by both thermal and moisture stress tests, the incorporation of a BTBT cation clearly significantly enhances the stability of the cesium lead(II) iodide black phase compared to the material system containing aliphatic BA cations. Next to

the characteristics of the individual BTBT cations, such as their pronounced rigidity as compared to the flexible BA cations, also the ordering of the BTBT cations in the organic layer of the perovskite could potentially contribute to the enhanced stability. Unfortunately, despite significant efforts, it was not possible to grow single crystals of the $n = 2$ (BTBT)₂CsPb₂I₇ perovskite to assess the ordering of the BTBT cations in the organic layer.

2.4. Time-Resolved Microwave Conductivity

To investigate the role of the molecular structure of the large organic cation in potentially contributing to the charge transport properties of the hybrid, TRMC measurements^[22,40,44] were performed on the spin-coated (BTBT)₂CsPb₂I₇ and (BA)₂CsPb₂I₇ thin films. In TRMC measurements, laser excitation induces mobile charge carriers leading to an increase in the photoconductivity of the thin films, which is measured as a function of time after photo-excitation. The product of the yield and mobility of the charges is related to the maximum photo-conductance (ΔG_{\max}) by^[22]

$$\phi \Sigma \mu = \frac{\Delta G_{\max}}{I_0 \beta e F_A} \quad (2)$$

where ϕ is the fraction of absorbed photons that leads to mobile charges, $\Sigma \mu = \mu_e + \mu_h$ is the total mobility of charge carriers, I_0 is the number of photons per unit area per pulse, β is the ratio of the inner dimensions of the microwave cell, e is the elementary charge, and F_A is the fraction of light absorbed by the sample at the excitation wavelength. **Figure 5** shows the time-resolved photoconductivity of the spin-coated (BTBT)₂CsPb₂I₇ and (BA)₂CsPb₂I₇ thin films.

Upon excitation, both TRMC traces show a sharp rise due to the generation of free mobile charge carriers. It is evident that the (BTBT)₂CsPb₂I₇ thin film shows a higher maximum $\phi \Sigma \mu$ (0.55 cm² V⁻¹ s⁻¹) compared to the reference (BA)₂CsPb₂I₇

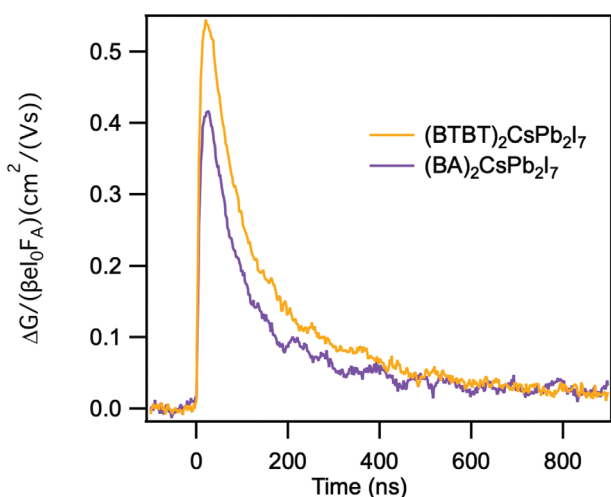


Figure 5. The product of the mobility and yield of charge carriers as a function of time upon photoexcitation with a 500 nm laser pulse with a photon intensity of $\approx 1.8 \times 10^{11}$ cm⁻². This product is directly proportional to that change in conductance on photoexcitation.^[55]

(0.42 cm² V⁻¹ s⁻¹). With the elapse of time, $\phi \Sigma \mu$ decays due to charge recombination or trapping.^[56] Both films show a very similar half-lifetime of the charge carriers of 95 ns and 90 ns for (BTBT)₂CsPb₂I₇ and (BA)₂CsPb₂I₇ thin films, respectively. Accordingly, we estimated the diffusion lengths of charge carriers ($L_D = \sqrt{D \tau_{1/2}}$ with $D = \frac{\mu k_B T}{e}$ and $\tau_{1/2}$ the half lifetime of the charge carriers) to be ≈ 0.35 and ≈ 0.3 μ m.

A plausible explanation for the observed similar lifetimes, and slightly higher $\phi \Sigma \mu$ for the (BTBT)₂CsPb₂I₇ thin film is that the incorporation of the BTBT molecules may slightly influence the exciton binding energy, thereby influencing the yield (ϕ) of dissociation of charges. Furthermore, the locally probed charge carrier mobility by microwaves,^[57,58] depends on the crystallinity in the film. Therefore, the larger microwave photoconductivity found in the (BTBT)₂CsPb₂I₇ film may also originate from higher film crystallinity. In summary, the polyheterocyclic aromatic BTBT ammonium cation has only a minor influence on the local charge carrier properties compared to the state-of-the-art BA cation. Therefore, we can conclude that using the BTBT cation, a material was obtained with significantly enhanced stability and comparable intrinsic charge transport properties compared to the reference BA cation.

2.5. Optoelectronic Device Properties

To test the performance of the (BTBT)₂CsPb₂I₇ quasi-2D hybrid perovskite with high crystallinity and stability in optoelectronic devices, we fabricated planar photoconductor-type detectors and evaluate their photo-response, EQE, and specific detectivity (D^*). The planar architecture was selected since the layered $n = 2$ hybrid perovskites show preferential growth parallel to the substrate surface.^[26] The device architecture consists of the respective perovskite film (thickness ≈ 200 nm, determined by profilometry) deposited onto a quartz substrate with an 80 nm thickness gold electrode evaporated on top of the thin films. A shadow mask with four interdigitating finger structures was employed to deposit the gold electrode (electrode distances $L = 0.05, 0.10, 0.25,$ and 0.50 mm; corresponding device area $A = 0.026, 0.048, 0.080,$ and 0.120 cm²; **Figure 6a**). The photocurrent is measured between the different interdigitating electrode fingers by sweeping an applied voltage between -15 and 15 V over them under a light intensity of 1 sun with a A.M. 1.5 G spectrum (ASTM). The I - V curves of the photoconductor-type detectors, (BTBT)₂CsPb₂I₇ and reference (BA)₂CsPb₂I₇, are evaluated under dark and light irradiation and presented in **Figure 6b,c**. Under light irradiation, the (BA)₂CsPb₂I₇ detector delivers photocurrents from 4.5×10^{-8} to 2×10^{-7} A at 15 V by decreasing the electrode distance L . This experimental trend is expected as, at the same voltage, the charge carrier transit time ($\tau_t = \frac{L^2}{\mu V}$) shortens, and thus, the amount of charge carrier

recombination events are reduced, resulting in an increased EQE for photoconductors.^[59] For the detector based on (BTBT)₂CsPb₂I₇, we observe a significant increase in light current by one order of magnitude, with photocurrents reaching almost 1.75×10^{-6} A at 15 V for the lowest electrode distance under light irradiation. Since only a slightly higher intrinsic

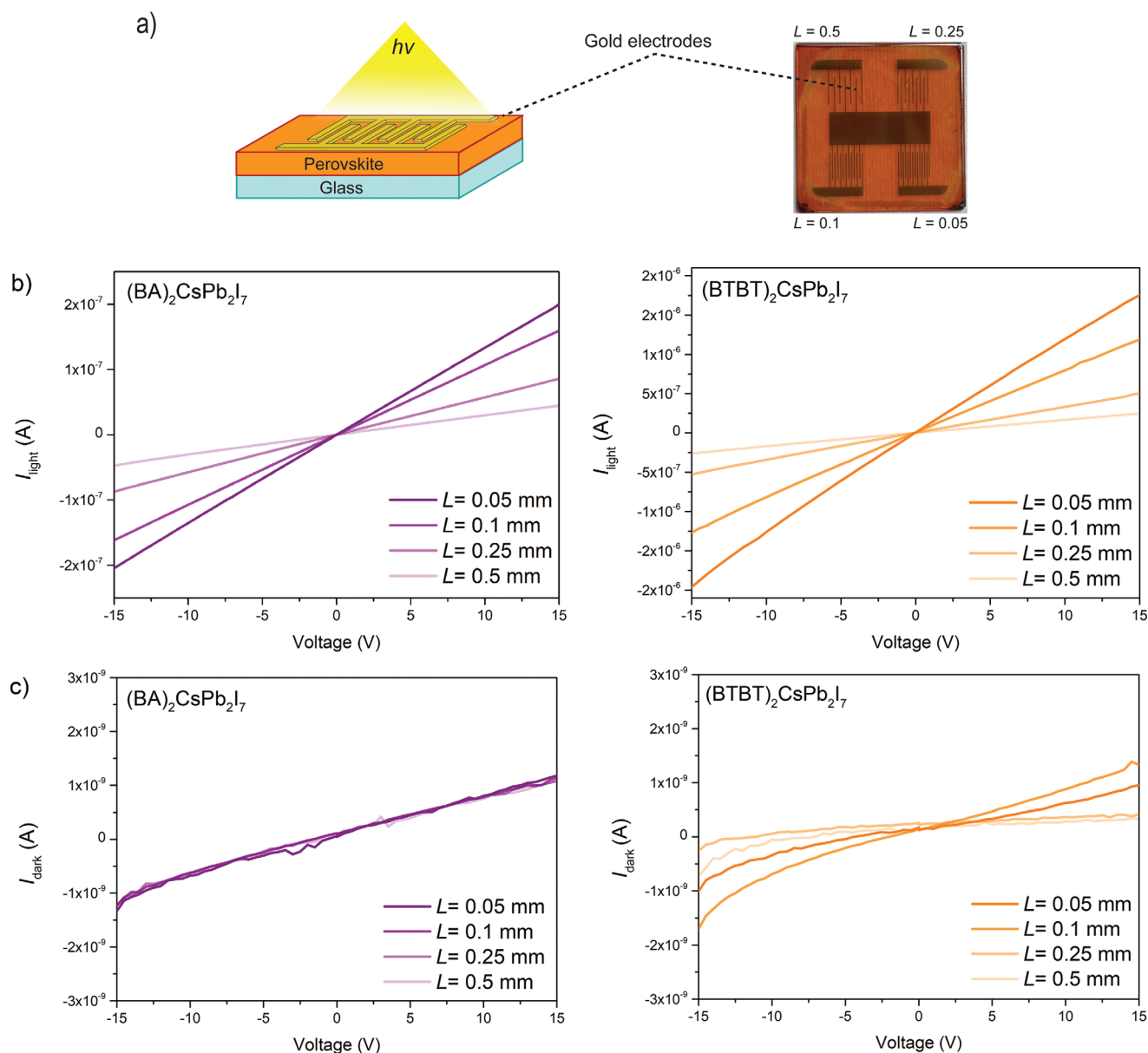


Figure 6. a) Schematic representation and photograph of the photoconductor-type detector. The I - V curves of the photoconductor-type detector based on $(\text{BA})_2\text{CsPb}_2\text{I}_7$, and $(\text{BTBT})_2\text{CsPb}_2\text{I}_7$, with different electrode distances $L = 0.05, 0.10, 0.25$, and 0.50 mm, under b) light irradiation and c) in the dark.

photoconductivity was found locally for $(\text{BTBT})_2\text{CsPb}_2\text{I}_7$ than for $(\text{BA})_2\text{CsPb}_2\text{I}_7$ by TRMC, we hypothesize that the substantial increase in photocurrent delivered by the $(\text{BTBT})_2\text{CsPb}_2\text{I}_7$ detector with respect to the BA-containing one, could be attributed to the larger crystallites in the thin film (vide supra). While TRMC probes the local (intragrain) charge carrier mobility, the photocurrent in photodetectors is determined by the macroscopic (intergrain) charge carrier mobility. Larger crystallites should lead to a reduced amount of grain boundaries.^[60]

The light to dark current ratio ($I_{\text{light}}/I_{\text{dark}}$) was estimated for each electrode distance, with $(\text{BTBT})_2\text{CsPb}_2\text{I}_7$ reaching the highest value of almost 2000 at a voltage bias of 15 V (Figure S11, Supporting Information). However, as the $I_{\text{light}}/I_{\text{dark}}$ ratio depends on the amount of light absorbed by the device,

a better detector performance metric is given by the specific detectivity D^* .

It is estimated based on the ratio of the responsivity ($R = \frac{\text{EQE} \times \lambda \times e}{hc}$), with EQE the EQE, λ the wavelength, e the elementary charge, h the Planck constant, and c speed of light) and the noise current (i_{noise}), assuming a bandwidth (Δf) near 1 Hz:^[61,62]

$$D^* (\text{Jones}) = \frac{R\sqrt{A\Delta f}}{i_{\text{noise}}} \quad (3)$$

The noise current was determined by considering the following noise sources: white shot and thermal noise.^[62,63] Flicker noise is neglected, which can be done when the devices

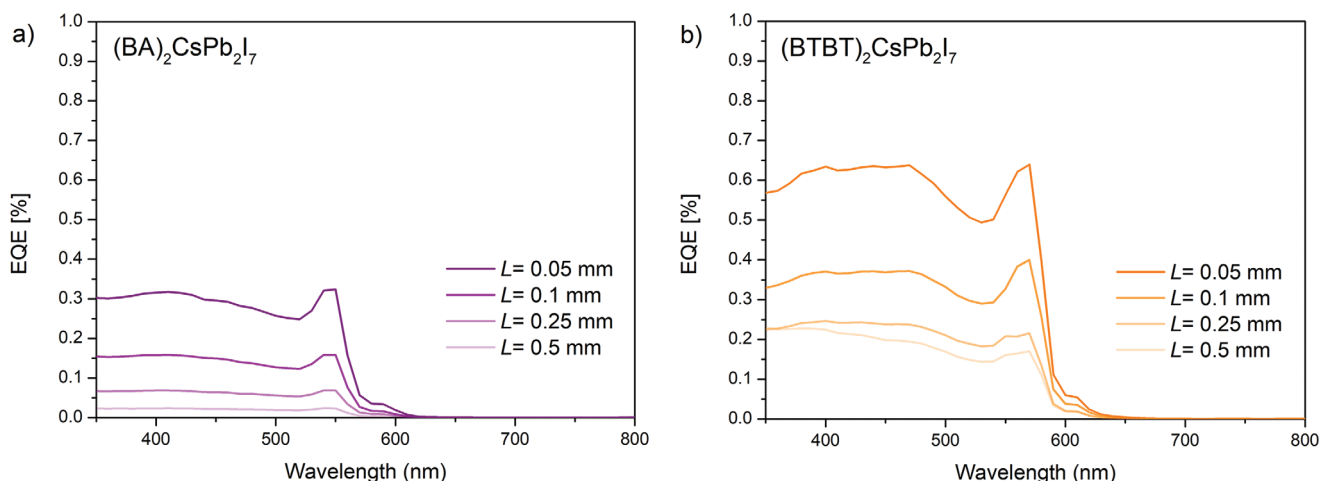


Figure 7. EQE spectra of the a) $(\text{BA})_2\text{CsPb}_2\text{I}_7$ and b) $(\text{BTBT})_2\text{CsPb}_2\text{I}_7$ detectors with different electrode distances $L = 0.05, 0.10, 0.25,$ and 0.50 mm, under a voltage bias of 10 V.

operate at a sufficiently high frequency.^[64] The white shot noise (i_{shot}) is linearly proportional to the dark current as it originates from the randomness of the amount of electrons moving from one end of the electrode to the other. On the other hand, the thermal noise (i_{thermal}) can be assessed by considering the total parallel resistance (R_p), which only consists of the shunt resistance (R_{shunt}) for a photoconductor-type detector:

$$i_{\text{noise}} = \sqrt{\langle i_{\text{shot}}^2 \rangle + \langle i_{\text{thermal}}^2 \rangle} = \sqrt{2eI_{\text{dark}}\Delta f + \frac{4kT}{R_{\text{shunt}}}\Delta f} \quad (4)$$

At a 10 V bias, the thermal noise component can be neglected, so only the white shot noise component contributes to the noise current to an appreciable extent.^[61,62]

EQE measurements were performed on the photoconductor-type detectors with different electrode distances at a 10 V voltage bias to determine their effectiveness of charge carrier collection at the Au electrodes (Figure 7). The EQE spectra expand over the range of 350 to 600 nm, peaking at their respective $n = 2$ excitonic absorption peak at 549 and 565 nm for $(\text{BA})_2\text{CsPb}_2\text{I}_7$, and $(\text{BTBT})_2\text{CsPb}_2\text{I}_7$, respectively. Here, the EQE intensity increases with decreasing electrode distance, which agrees with the delivered photocurrents gathered from the I - V measurements. Remarkably, the EQE values of the $(\text{BTBT})_2\text{CsPb}_2\text{I}_7$ -based detector are almost doubled with respect to the $(\text{BA})_2\text{CsPb}_2\text{I}_7$ -based one, again likely attributed to the larger crystallites and therefore reduced grain boundaries within the $(\text{BTBT})_2\text{CsPb}_2\text{I}_7$ thin film. The EQE spectra of 3 different devices are shown in Figure S12, Supporting Information.

The specific detectivity D^* was determined for each quasi-2D hybrid perovskite detector with the smallest electrode distance $L = 0.05$ mm and a respective device area A of 0.026 cm² (Figure 8).

Our $(\text{BTBT})_2\text{CsPb}_2\text{I}_7$ -based detectors show a similar specific detectivity D^* compared to the state-of-the-art BA-based detectors. Although the photocurrent and EQE are higher for the BTBT-based detectors, the dark current is slightly higher for these detectors compared to the BA-based ones, resulting in similar values for the specific detectivity.

3. Conclusions

In conclusion, we demonstrated the potential of using a tailored polyheterocyclic aromatic BTBT cation in efficiently stabilizing the cesium lead(II) iodide black phase through dimension engineering of a quasi-2D hybrid perovskite $(\text{BTBT})_2\text{CsPb}_2\text{I}_7$. In situ temperature-controlled XRD showed the vastly superior thermal stability of the $(\text{BTBT})_2\text{CsPb}_2\text{I}_7$ thin film compared to the state-of-the-art butylammonium (BA)-based $(\text{BA})_2\text{CsPb}_2\text{I}_7$ thin film. Moreover, the moisture stability of the thin films was monitored by XRD and UV-vis spectroscopy. Here, the $(\text{BTBT})_2\text{CsPb}_2\text{I}_7$ thin film displayed excellent phase stability for 152 days when exposed to 77% RH at room temperature in the dark, whereas the $(\text{BA})_2\text{CsPb}_2\text{I}_7$ thin film showed significant degradation already after a single day. Therefore, we have clearly illustrated the benefit of inserting a more rigid, hydrophobic polyheterocyclic aromatic cation instead of a flexible aliphatic one, in greatly enhancing the structural integrity of the

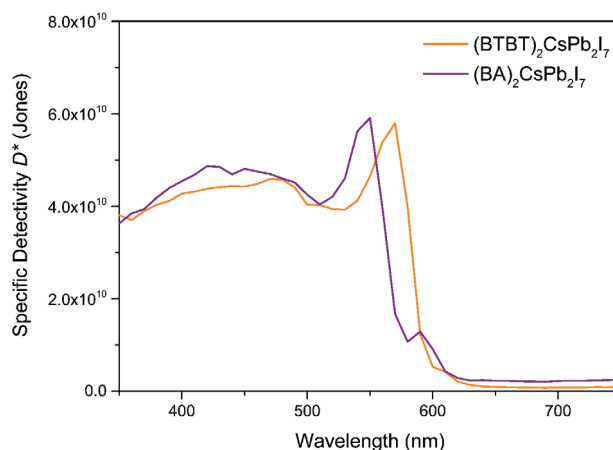


Figure 8. Specific detectivity D^* of a $(\text{BA})_2\text{CsPb}_2\text{I}_7$ and $(\text{BTBT})_2\text{CsPb}_2\text{I}_7$ photoconductor-type detector as a function of wavelength, with electrode distance $L = 0.05$ mm. To assess device reproducibility, three detectors were prepared for each perovskite film (Figure S13, Supporting Information), the average value of the 3 curves of the 3 devices is shown here.

quasi-2D hybrid perovskite and inhibiting degradation toward the undesirable, photoinactive yellow δ -phase or lead(II) iodide.

By performing TRMC measurements, a slightly higher local microwave photoconductivity in the $(\text{BTBT})_2\text{CsPb}_2\text{I}_7$ thin film was measured compared to the $(\text{BA})_2\text{CsPb}_2\text{I}_7$ thin film, yielding slightly longer charge carrier diffusion lengths. Photoconductor-type detectors based on $(\text{BTBT})_2\text{CsPb}_2\text{I}_7$ demonstrated a significant increase in photocurrent and EQE and a similar specific detectivity as compared to the BA-based detectors. Future research will focus on clarifying the relationship between the rigidity of the large organic ammonium cation and the intrinsic and device stability of the quasi-2D hybrid perovskite.

4. Experimental Section

Chemicals and Reagents: Lead iodide (PbI_2 , 99.999%) was obtained from Lumtec and cesium iodide (99.999% trace metals basis) was purchased at Merck. Hydroiodic acid (HI, 57% w/w aq., distilled, unstabilized), sodium hydrosulfide hydrate ($\text{NaSH}\cdot x\text{H}_2\text{O}$), 3-chloropropanoyl chloride, aluminum trichloride (AlCl_3), methyl sulfoxide (DMSO, 99.7%, extra dry), *N,N*-dimethylacetamide (DMAC, 99.5%, extra dry) and lithium aluminum hydride (LiAlH_4) were purchased from Acros Organics and used as received. 2-Chlorobenzaldehyde (99%) was purchased from Fisher Scientific. Sodium diformylamide (>97%) and butyl ammonium iodide (BAI, 97%) were purchased from TCI. For purification, BAI was dissolved in MeOH (4 mL) and poured into Et_2O (200 mL). The resulting precipitate was dried under vacuum to afford BAI as a white product before use. HCl (37%) was purchased from VWR. All solvents and reagents were used as received. The dry DMF that was used to make the precursor solutions, dichloromethane (DCM), toluene, and diethyl ether (Et_2O) were obtained from a solvent purification system (MBRAUN SPS-800). All other solvents (reagent grade) were purchased from Fisher Scientific.

Thin-Film Deposition: All precursor solutions were filtered through a PTFE syringe filter (0.45 μm mesh) before use. Quartz substrates were cleaned through successive sonication steps in the following order of solvents (detergent water, deionized water, acetone, and isopropanol; 15 min for each step), followed by a UV-ozone treatment of 15 min. The precursor solutions were deposited as thin films on quartz substrates by spin coating via a one-step method and annealed (thermal or solvent vapor annealing) on a hotplate in a glove box under a nitrogen atmosphere (< 0.1 ppm O_2 , < 0.1 ppm H_2O). Afterward, the samples were stored in a glovebox and only removed for analysis.

$(\text{BA})_2\text{CsPb}_2\text{I}_7$: Stoichiometric amounts of butylamine hydroiodide (BAI), cesium iodide (CsI), and PbI_2 were dissolved in dry DMF:DMAC 8:2 (0.3 M) under continuous stirring at 65 °C for 30 min. The thin films were thermally annealed at 130 °C for 10 min. Spin coating: 2000 rpm, 2000 rpm s^{-1} , 20 s.

$(\text{BTBT})_2\text{CsPb}_2\text{I}_7$: Stoichiometric amounts of the BTBT iodide salt, cesium iodide (CsI), and PbI_2 were dissolved in dry DMF:DMSO 9:1 (0.3 M) under continuous stirring at 65 °C for 30 min. The thin films were solvent vapor annealed at 210 °C for 5 min. In this method, a 15 μL droplet of dry DMSO was put on the inner wall of a petri dish. When the thin film was covered by the petri dish on the hot plate, the droplet evaporates and generates a DMSO-containing atmosphere for the film during thermal annealing. Afterward, the crystalline thin film was removed from the hot plate. Spin coating: 2000 rpm, 2000 rpm s^{-1} , 20 s.

The same processing conditions were applied to the films used for the in situ measurements.

Characterization: The samples for the moisture stability measurements were stored in a desiccator with a saturated NaCl solution. The RH was measured using a humidity sensor.

Optical absorption spectra were measured on a Cary 5000 UV-vis-NIR spectrophotometer from Agilent Technologies; a cleaned quartz substrate was used as a calibration background.

PL experiments were performed at room temperature under excitation with a 405 nm pulsed diode laser (Thorlabs, NPL41C, 6 ns pulse length, and 4.1 nJ pulse $^{-1}$). Backscattered PL emission was diffracted in a grating spectrograph (Andor, Kymera 328i-D2-SIL) and registered by a linear CCD detector (Andor, iDus 416-LDC-DD). Unwanted laser reflections were eliminated from the spectrum by means of a 474 nm long-wavelength pass color filter in front of the spectrograph entrance. In order to avoid photo-degradation, the devices were mounted in N_2 atmosphere in an airtight sample holder. All spectra were corrected for the spectral response of the set-up determined using a calibrated light source (Avantes, AvaLight-HAL-CAL-Mini).

X-ray diffraction measurements on thin films were performed at room temperature in ambient atmosphere on a Bruker D8 Discover diffractometer with a parallel beam geometry using a Göbel mirror and $\text{CuK}\alpha$ radiation, with a 1D detector (Lynxeye). In situ XRD measurements were carried out on a Bruker D8 Discover XRD system equipped with a Cu X-ray source ($\lambda = 1.5406 \text{ \AA}$) and a linear X-ray detector. The samples were put on a sample heating stage inside a closed annealing chamber. The XRD measurements were carried out under N_2 atmosphere with a continuous nitrogen flow rate of 500 sccm at atmospheric pressure. Samples were heated via a stepwise temperature profile from RT up to 290 °C in steps of 10 °C. The temperature was measured with a K-type thermocouple. Every 10 °C the temperature was stabilized for several seconds before an XRD scan from 2–35° in 2 theta was taken at that specific temperature.

Thermogravimetric analysis was performed on a Q500 analyzer from TA instruments using a Pt sample cup with a temperature profile of 10 °C min^{-1} under a N_2 flow of 100 mL min^{-1} .

TRMC measurements were performed at room temperature with pulsed laser excitation (repetition rate 10 Hz) at 500 nm. The photon intensities were determined using a laser power/energy meter (LabMax-TOP) and the optical densities of the neutral density filters. During the experiment, the thin films (1.5 cm x 2.1 cm) were placed in a sealed microwave cell under dry nitrogen atmosphere to prevent sample degradation. The temporal resolution was limited by the width of the laser pulse (3.5 ns) and the response time of the system (18 ns). The fraction of absorbed light (F_A) at 500 nm was determined from the UV/vis absorption spectrum.

The thin film thicknesses were determined using a Bruker DektakXT profilometer.

SEM measurements were performed on a Zeiss GeminiSEM 450. The AFM measurements were performed with a JPK NanoWizard 3 AFM (JPK Instruments AG, Berlin, Germany) using AC mode under ambient atmosphere. AppNano Silicon ACTA-50 tips with a cantilever length $\approx 125 \text{ nm}$, spring constant $\approx 40 \text{ N m}^{-1}$, and resonance frequency $\approx 300 \text{ kHz}$ were utilized. The scan angle, set point height, gain values, and scan rate were corrected according to the AFM tip calibration.

Contact angle measurements were performed on a Dataphysics Model OCA 15 Plus Optical Contact Angle Measuring and Contour Analysis System. Measurements were performed using 2 μL drops of demineralized water.

Devices were made by spin coating films of a $(\text{BA})_2\text{MAPb}_2\text{I}_7$, $(\text{BA})_2\text{CsPb}_2\text{I}_7$, and $(\text{BTBT})_2\text{CsPb}_2\text{I}_7$ precursor solution (prepared as described above) on quartz substrates, followed by either thermal annealing or solvent vapor annealing. On top of the resulting film, 80 nm of Au was evaporated through a shadow mask to obtain electrodes with interdigitating finger structures. Next, silver paste was applied to the edges of the substrate to make electrical contact between the evaporated Au electrode and the pins of the measuring cell. The devices were measured from -15 V till +15 V in steps of 0.5 V, either in the dark or under 1 sun A.M 1.5G illumination. The *I*-*V* curves in darkness of all photoconductor-type detectors were evaluated using a Keithley 2400 source meter. EQE measurements were performed using a homebuilt setup with a Newport Apex illuminator (100 W Quartz Tungsten Halogen lamp) as light source and a Newport Cornerstone 130° monochromator. A chopper frequency of 135 Hz was applied on the monochromated light and the photocurrent was measured using a Stanford SR830 lock-in amplifier. The signal was pre-amplified using a DLPCA-200 amplifier from FEMTO, under 10 V (amplification 10^6 , full bandwidth, DC mode).

Supporting Information

Supporting Information is available from the Wiley Online Library or from the author.

Acknowledgements

P.-H.D. is a special research fund (BOF) doctoral (Ph.D.) student at UHasselt/IMO. M.M. and A.M. are SB Ph.D. fellows at FWO (No. 1S20118N and No. 1115721N respectively). W.T.M.V.G., M.V.L., L.L., K.V., and D.V. acknowledge the FWO for the funding of the SBO project PROCEED (FWOS002019N) and the senior FWO research project G043320N. S.M. is a BOF (Ph.D.) student at UHasselt/IMO (grant nr. BOF19OWB15). S.G. acknowledges the Research Foundation – Flanders (FWO Vlaanderen) for funding his Ph.D. fellowship. D.D. and C.D. acknowledge FWO-Vlaanderen and the Special Research Fund BOF of Ghent University (GOA project, Grant No. 01G01019) for funding. Z.W. and F.G. acknowledge the project “Chirality-induced spin selectivity in electron transport” (project nr. 680.92.18.01) of the research programme “Natuurkunde Vrije Programmas,” which was (partly) financed by the Dutch Research Council (NWO) and of which this publication is a part. The work has been carried out in the context of the Solliance network (<http://www.solliance.eu>), from which UHasselt is a member. Additionally, UHasselt is a partner in the Energyville Consortium (<http://www.energyville.be/about-energyville>).

Conflict of Interest

The authors declare no conflict of interest.

Data Availability Statement

The data that support the findings of this study are available in the supplementary material of this article.

Keywords

cesium black phase stabilization, low-dimensional perovskites, moisture stability, photodetectors, thermal stability

Received: April 12, 2022

Revised: May 18, 2022

Published online: June 24, 2022

- [1] M. K. Assadi, S. Bakhoda, R. Saidur, H. Hanaei, *Renewable Sustainable Energy Rev.* **2018**, *81*, 2812.
- [2] C. R. Dong, Y. Wang, K. Zhang, H. Zeng, *EnergyChem* **2020**, *2*, 100026.
- [3] NREL, *Efficiency chart*, **2022**, <https://www.nrel.gov/pv/cell-efficiency.html>.
- [4] R. L. Milot, R. J. Sutton, G. E. Eperon, A. A. Haghighirad, J. Martinez Hardigree, L. Miranda, H. J. Snaith, M. B. Johnston, L. M. Herz, *Nano Lett.* **2016**, *16*, 7001.
- [5] B. Conings, J. Drijkoningen, N. Gauquelin, A. Babayigit, J. D’Haen, L. D’Ollieslaeger, A. Ethirajan, J. Verbeeck, J. Manca, E. Mosconi, F. De Angelis, H.-G. Boyen, *Adv. Energy Mater.* **2015**, *5*, 1500477.
- [6] T. A. Berhe, W.-N. Su, C.-H. Chen, C.-J. Pan, J.-H. Cheng, H.-M. Chen, M.-C. Tsai, L.-Y. Chen, A. A. Dubale, B.-J. Hwang, *Energy Environ. Sci.* **2016**, *9*, 323.
- [7] L. Gu, D. Zhang, M. Kam, Q. Zhang, S. Poddar, Y. Fu, X. Mo, Z. Fan, *Nanoscale* **2018**, *10*, 15164.
- [8] D. Thrithamarassery Gangadharan, D. Ma, *Energy Environ. Sci.* **2019**, *12*, 2860.
- [9] G. E. Eperon, S. D. Stranks, C. Menelaou, M. B. Johnston, L. M. Herz, H. J. Snaith, *Energy Environ. Sci.* **2014**, *7*, 982.
- [10] D. Wang, M. Wright, N. K. Elumalai, A. Uddin, *Sol. Energy Mater. Sol. Cells* **2016**, *147*, 255.
- [11] R. J. Sutton, G. E. Eperon, L. Miranda, E. S. Parrott, B. A. Kamino, J. B. Patel, M. T. Hörantner, M. B. Johnston, A. A. Haghighirad, D. T. Moore, H. J. Snaith, *Adv. Energy Mater.* **2016**, *6*, 1502458.
- [12] G. E. Eperon, G. M. Paternò, R. J. Sutton, A. Zampetti, A. A. Haghighirad, F. Cacialli, H. J. Snaith, *J. Mater. Chem. A* **2015**, *3*, 19688.
- [13] R. E. Beal, D. J. Slotcavage, T. Leijtens, A. R. Bowering, R. A. Belisle, W. H. Nguyen, G. F. Burkhard, E. T. Hoke, M. D. McGehee, *J. Phys. Chem. Lett.* **2016**, *7*, 746.
- [14] F. Bella, P. Renzi, C. Cavallo, C. Gerbaldi, *Chem. - Eur. J.* **2018**, *24*, 12183.
- [15] T. Zhang, M. I. Dar, G. Li, F. Xu, N. Guo, M. Grätzel, Y. Zhao, *Sci. Adv.* **2017**, *3*, e1700841.
- [16] A. Marronnier, G. Roma, S. Boyer-Richard, L. Pedesseau, J.-M. Jancu, Y. Bonnassieux, C. Katan, C. C. Stoumpos, M. G. Kanatzidis, J. Even, *ACS Nano* **2018**, *12*, 3477.
- [17] Y. Wang, Y. Chen, T. Zhang, X. Wang, Y. Zhao, *Adv. Mater.* **2020**, *32*, 2001025.
- [18] C. C. Stoumpos, C. D. Malliakas, J. A. Peters, Z. Liu, M. Sebastian, J. Im, T. C. Chasapis, A. C. Wibowo, D. Y. Chung, A. J. Freeman, B. W. Wessels, M. G. Kanatzidis, *Cryst. Growth Des.* **2013**, *13*, 2722.
- [19] J. B. Hoffman, A. L. Schleper, P. V. Kamat, *J. Am. Chem. Soc.* **2016**, *138*, 8603.
- [20] P. Luo, W. Xia, S. Zhou, L. Sun, J. Cheng, C. Xu, Y. Lu, *J. Phys. Chem. Lett.* **2016**, *7*, 3603.
- [21] R. F. Kahwagi, S. T. Thornton, B. Smith, G. I. Koleilat, *Front. Optoelectron.* **2020**, *13*, 196.
- [22] R. Herckens, W. T. M. Van Gompel, W. Song, M. C. Gélvez-Rueda, A. Maufort, B. Ruttens, J. D’Haen, F. C. Grozema, T. Aernouts, L. Lutsen, D. Vanderzande, *J. Mater. Chem. A* **2018**, *6*, 22899.
- [23] W. T. M. Van Gompel, R. Herckens, M. Mertens, P. Denis, B. Ruttens, J. D’Haen, K. Van Hecke, L. Lutsen, D. Vanderzande, *ChemNanoMat* **2021**, *7*, 1013.
- [24] P.-H. Denis, M. Mertens, W. T. M. Van Gompel, K. Van Hecke, B. Ruttens, J. D’Haen, L. Lutsen, D. Vanderzande, *Chem. Mater.* **2021**, *33*, 5177.
- [25] C. C. Stoumpos, D. H. Cao, D. J. Clark, J. Young, J. M. Rondinelli, J. I. Jang, J. T. Hupp, M. G. Kanatzidis, *Chem. Mater.* **2016**, *28*, 2852.
- [26] D. H. Cao, C. C. Stoumpos, O. K. Farha, J. T. Hupp, M. G. Kanatzidis, *J. Am. Chem. Soc.* **2015**, *137*, 7843.
- [27] J.-F. Liao, H.-S. Rao, B.-X. Chen, D.-B. Kuang, C.-Y. Su, *J. Mater. Chem. A* **2017**, *5*, 2066.
- [28] Y. Jiang, J. Yuan, Y. Ni, J. Yang, Y. Wang, T. Jiu, M. Yuan, J. Chen, *Joule* **2018**, *2*, 1356.
- [29] C. C. Stoumpos, C. M. M. Soe, H. Tsai, W. Nie, J.-C. Blancon, D. H. Cao, F. Liu, B. Traoré, C. Katan, J. Even, A. D. Mohite, M. G. Kanatzidis, *Chem* **2017**, *2*, 427.
- [30] M. Zhou, C. Fei, J. S. Sarmiento, H. Wang, *Sol. RRL* **2019**, *3*, 1800359.
- [31] A. H. Proppe, R. Quintero-Bermudez, H. Tan, O. Voznyy, S. O. Kelley, E. H. Sargent, *J. Am. Chem. Soc.* **2018**, *140*, 2890.
- [32] J. Liu, J. Leng, K. Wu, J. Zhang, S. Jin, *J. Am. Chem. Soc.* **2017**, *139*, 1432.
- [33] A. Hadi, B. J. Ryan, R. D. Nelson, K. Santra, F. Lin, E. W. Cochran, M. G. Panthani, *Chem. Mater.* **2019**, *31*, 4990.

- [34] W. T. M. Van Gompel, R. Herckens, K. Van Hecke, B. Ruttens, J. D'Haen, L. Lutsen, D. Vanderzande, *Chem. Commun.* **2019**, 55, 2481.
- [35] M. D. Smith, B. A. Connor, H. I. Karunadasa, *Chem. Rev.* **2019**, 119, 3104.
- [36] K. Jemli, P. Audebert, L. Galmiche, G. Trippé-Allard, D. Garrot, J.-S. Lauret, E. Deleporte, *ACS Appl. Mater. Interfaces* **2015**, 7, 21763.
- [37] X. Li, J. Yang, Z. Song, R. Chen, L. Ma, H. Li, J. Jia, J. Meng, X. Li, M. Yi, X. Sun, *ACS Appl. Energy Mater.* **2018**, 1, 4467.
- [38] C. Ortiz-Cervantes, P. I. Román-Román, J. Vazquez-Chavez, M. Hernández-Rodríguez, D. Solís-Ibarra, *Angew. Chem., Int. Ed.* **2018**, 57, 13882.
- [39] J. V. Passarelli, D. J. Fairfield, N. A. Sather, M. P. Hendricks, H. Sai, C. L. Stern, S. I. Stupp, *J. Am. Chem. Soc.* **2018**, 140, 7313.
- [40] M. C. Gélvez-Rueda, W. T. M. Van Gompel, R. Herckens, L. Lutsen, D. Vanderzande, F. C. Grozema, *J. Phys. Chem. Lett.* **2020**, 11, 824.
- [41] N. Marchal, W. Van Gompel, M. C. Gélvez-Rueda, K. Vandewal, K. Van Hecke, H.-G. Boyen, B. Conings, R. Herckens, S. Maheshwari, L. Lutsen, C. Quarti, F. C. Grozema, D. Vanderzande, D. Beljonne, *Chem. Mater.* **2019**, 31, 6880.
- [42] M. Van Landeghem, W. Van Gompel, R. Herckens, L. Lutsen, D. Vanderzande, S. Van Doorslaer, E. Goovaerts, *J. Phys. Chem. C* **2021**, 125, 18317.
- [43] C. Niebel, Y. Kim, C. Ruzié, J. Karpinska, B. Chattopadhyay, G. Schweicher, A. Richard, V. Lemaur, Y. Olivier, J. Cornil, A. R. Kennedy, Y. Diao, W.-Y. Lee, S. Mannsfeld, Z. Bao, Y. H. Geerts, *J. Mater. Chem. C* **2015**, 3, 674.
- [44] W. T. M. Van Gompel, R. Herckens, P.-H. Denis, M. Mertens, M. C. Gélvez-Rueda, K. Van Hecke, B. Ruttens, J. D'Haen, F. C. Grozema, L. Lutsen, D. Vanderzande, *J. Mater. Chem. C* **2020**, 8, 7181.
- [45] K. Du, Q. Tu, X. Zhang, Q. Han, J. Liu, S. Zauscher, D. B. Mitzi, *Inorg. Chem.* **2017**, 56, 9291.
- [46] M. Yuan, L. N. Quan, R. Comin, G. Walters, R. Sabatini, O. Voznyy, S. Hoogland, Y. Zhao, E. M. Beauregard, P. Kanjanaboos, Z. Lu, D. H. Kim, E. H. Sargent, *Nat. Nanotechnol.* **2016**, 11, 872.
- [47] A. Vassilakopoulou, D. Papadatos, I. Zakouras, I. Koutselas, *J. Alloys Compd.* **2017**, 692, 589.
- [48] W. Peng, J. Yin, K.-T. Ho, O. Ouellette, M. De Bastiani, B. Murali, O. El Tall, C. Shen, X. Miao, J. Pan, E. Alarousu, J.-H. He, B. S. Ooi, O. F. Mohammed, E. Sargent, O. M. Bakr, *Nano Lett.* **2017**, 17, 4759.
- [49] Z.-H. Zheng, H.-B. Lan, Z.-H. Su, H.-X. Peng, J.-T. Luo, G.-X. Liang, P. Fan, *Sci. Rep.* **2019**, 9, 17422.
- [50] Z. Song, S. C. Wathage, A. B. Phillips, B. L. Tompkins, R. J. Ellingson, M. J. Heben, *Chem. Mater.* **2015**, 27, 4612.
- [51] Y. Fu, M. T. Rea, J. Chen, D. J. Morrow, M. P. Hautzinger, Y. Zhao, D. Pan, L. H. Manger, J. C. Wright, R. H. Goldsmith, S. Jin, *Chem. Mater.* **2017**, 29, 8385.
- [52] E. Amerling, S. Baniya, E. Lafalce, C. Zhang, Z. V. Vardeny, L. Whittaker-Brooks, *J. Phys. Chem. Lett.* **2017**, 8, 4557.
- [53] W. T. M. Van Gompel, R. Herckens, K. Van Hecke, B. Ruttens, J. D'Haen, L. Lutsen, D. Vanderzande, *ChemNanoMat* **2019**, 5, 323.
- [54] H. Zheng, G. Liu, L. Zhu, J. Ye, X. Zhang, A. Alsaedi, T. Hayat, X. Pan, S. Dai, *Adv. Energy Mater.* **2018**, 8, 1800051.
- [55] T. J. Savenije, A. J. Ferguson, N. Kopidakis, G. Rumbles, *J. Phys. Chem. C* **2013**, 117, 24085.
- [56] M. C. Gélvez-Rueda, M. B. Fridriksson, R. K. Dubey, W. F. Jager, W. van der Stam, F. C. Grozema, *Nat. Commun.* **2020**, 11, 1901.
- [57] O. G. Reid, M. Yang, N. Kopidakis, K. Zhu, G. Rumbles, *ACS Energy Lett.* **2016**, 1, 561.
- [58] T. J. Savenije, D. Guo, V. M. Caselli, E. M. Hutter, *Adv. Energy Mater.* **2020**, 10, 1903788.
- [59] R. H. Kingston, in *Encyclopedia of Physical Science and Technology*, Elsevier, Amsterdam **2003**, p. 237.
- [60] Z. Liu, D. Liu, H. Chen, L. Ji, H. Zheng, Y. Gu, F. Wang, Z. Chen, S. Li, *Nanoscale Res. Lett.* **2019**, 14, 304.
- [61] Y. Fang, A. Armin, P. Meredith, J. Huang, *Nat. Photonics* **2019**, 13, 1.
- [62] S. Gielen, C. Kaiser, F. Verstraeten, J. Kublitski, J. Benduhn, D. Spoltore, P. Verstappen, W. Maes, P. Meredith, A. Armin, K. Vandewal, *Adv. Mater.* **2020**, 32, 2003818.
- [63] S. M. Sze, K. K. Ng, *Physics of Semiconductor Devices*, 3rd ed., Wiley, New York **2006**.
- [64] V. Venugopalan, R. Sorrentino, P. Topolovsek, D. Nava, S. Neutzner, G. Ferrari, A. Petrozza, M. Caironi, *Chem* **2019**, 5, 868.